Electrostatic structure of a magnetized laser-produced plasma

Jeffrey Bonde, Stephen Vincena, and Walter Gekelman

Department of Physics and Astronomy, University of California, Los Angeles, Los Angeles, California 90095, USA

Measurements of the structure of the electrostatic fields produced by the expansion of a laser-produced plasma into a background magnetized plasma are presented. The three-dimensional measurements of the electrostatic field are made using an emissive probe that measures the time-varying plasma potential on two orthogonal planes, one across and one containing the background magnetic field. The inductive electric field is also calculated from probe measurements of the time-varying magnetic fields. Deviations from local charge neutrality at the level of 10^{-4} generate a radial electrostatic field with peak strength an order of magnitude larger than the corresponding inductive field. The electrostatic energy density near full expansion is over an order of magnitude larger than that of the induced azimuthal electric field. These measurements show that electrostatic fields must be included in theoretical and computational models of collisionless coupling in magnetized point explosions of laser-produced plasmas and their relation to similar phenomena such as magnetospheric chemical releases.

PACS number(s): 52.38.Mf, 52.50.Jm, 52.55.Dy

Introduction. Laser-produced diamagnetic cavities have been studied now for several decades [1–4]. They can mimic structures as varied as chemical releases in space [the Active Magnetospheric Particle Tracer Explorers mission (AMPTE)] [5], high-altitude explosions [6,7], comets [8], and the solar wind [9] (International Sun-Earth Explorer spacecraft). Their significance with regard to space phenomena has received extensive attention [10–14] including work on surface instabilities [15–17], radiated waves [4,18], and collisionless shock formation [19–21]. The AMPTE experiments, laser-produced plasmas (LPPs), and high-altitude explosions are related in that they all have high kinetic ram pressures with typical values ($p_{\text{ram}}2\mu_0/B^2$) being $\sim 10^8$ (AMPTE), $\sim 10^{15}$ (high-altitude explosions), and $10^3 - 10^7$ (LPPs). The expansion velocities v_{exp} of these three are high enough that collisionless mechanisms play a role in interactions with a tenuous ambient plasma. An unsolved mystery is how the collisionless expanding plasma couples to an ambient plasma. Previous experiments using Doppler shifts along with results from hybrid code simulations indicated that the background plasma is pushed out of the way by the LPP through induced electric fields. In this work we show that the coupling is due to electrostatic fields (an order of magnitude larger than the induced fields in this case) that are set up during the expansion.

In situ measurements of the three-dimensional (3D) electrostatic field structure of an LPP are presented. Propagation of the fields along and across the background magnetic field is presented. Charge density is derived from the 3D electric fields and shows a charge layer at the edge of the cavity.

Setup. A schematic of the experimental setup is given in Fig. 1. The LPP is generated by irradiating the surface of a cylindrical graphite target rod using a focused 8-ns, 1064-nm, 1-J Nd:YAG laser pulse, with spot radius $r_s = 250\,\mu$m. To reduce cratering, the target is rotated to a clean surface every five laser shots and translated ($-\hat{y}$) upon a full rotation. The target is suspended in the vacuum chamber ($D = 1$ m and $L = 20$ m) of the upgraded Large Plasma Device (LaPD) [22]. The device generates a pulsed (10-ms) magnetized ($B_0 = -750\,G\hat{z}$) argon plasma using two thermionic cathode discharges. The first cathode ($z = 5.4$ m) produces a 10-cm-diam column [23] positioned such that the target region is in the center of the

column. Swept Langmuir probes yield an ambient density $n_e = 4 \times 10^{12}\,\text{cm}^{-3}$ and electron temperature $T_e = 8$ eV. The probe is calibrated using a microwave interferometer. The Ar^+ temperature (measured using laser-induced fluorescence in a previous experiment under similar conditions) is 4 eV. The plasma from the second cathode (at $z = -9.7$ m, $D = 60$ cm, $n_e = 1 \times 10^{12}\,\text{cm}^{-3}$, and $T_e = 4$ eV) serves to reduce pressure-gradient instabilities in the primary column. With this setup, the ambient plasma properties are reproducible within 10% for each discharge. The laser and cathodes operate with a one-second cadence, allowing collection of ensemble data sets.

Embedded within a magnetic field, the LPPs expand freely [24,25] until the initial free energy has been expended in expulsion of the background magnetic field. This gives the cavity a characteristic radius R_b corresponding to stagnation and a characteristic time of peak diamagnetism $\tau_D \sim R_b/v_{\text{exp}}$. Here the LPP expands at $v_{\text{exp}} = 1.3 \pm 0.2 \times 10^7$ cm/s $= v_A = 24\,c_s$, where v_A and c_s are, respectively, the background plasma Alfvén and sound speeds. The expansion speed is determined from CCD camera images ($\Delta t \geqslant 3$ ns) looking across the magnetic field and particle time-of-flight probe diagnostics and is in agreement with theoretical scaling laws [26] ($v_{\text{theory}} = 1.28 \times 10^7$ cm/s). The orderings of the physical scale lengths of the LPP-ambient system are $r_s \ll R_b$ (2 cm) $\ll R_{ci}$ (22 cm) $< c/\omega_{pi}$ (72 cm) $\ll \lambda_{ii}$ (~ 1 km), where R_{ci} is the directed Larmor radius of the carbon ions across the field, ω_{pi} is the argon ion plasma frequency, and λ_{ii} is the LPP ion-ambient ion mean free path. Note the relationship between the parameters R_b and r_s: $p_{\text{ram}}2\mu_0/B^2 \sim (R_b/r_s)^3$. Under these conditions, the debris ions can be modeled kinetically as single particles moving through the LPP's self-consistent fields.

The electromagnetic fields are measured with emissive [27] and magnetic induction probes. In Fig. 1 the probes come in from the $-x$ direction and have areas of about 0.75 and 1 mm^2, respectively. The probe signals are digitized at 1.25 GHz with 10-bit resolution. Output from a fast photodiode is digitized to provide a timing reference, defining $t = 0$ when the laser strikes the target. Probe data are acquired for ten laser shots after which the probe is moved via computer control to the next location in the data plane and the process is repeated.
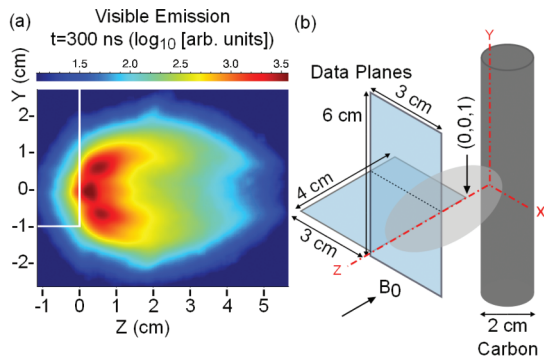
FIG. 1. (Color) (a) False color visible light emission with carbon target drawn in white and (b) cartoon rendering of the experimental arrangement. Blue planes depict planes in which data were acquired with $\delta x = \delta z = \delta y = 2$ mm resolution. The origin is taken to be the laser focal point. The laser enters $\sim 30°$ from the z axis in the xz plane, on the side away from the diagnostic planes. The transparent ellipsoid denotes the approximate size of the LPP at the time of peak diamagnetism: $\tau_D = 240$ ns.

Results. The main features of the electric field structure in the xy plane generated by the expansion are displayed in Fig. 2 at two select times. The earlier time [Fig. 2(a)] is after the axial boundary of the LPP passes through the diagnostic plane at $z = 2$ cm but before the time of peak diamagnetism. The later time [Fig. 2(b)] shows the electrostatic field at peak diamagnetism $\tau_d = 240$ ns.

Similar to that predicted in magnetospheric barium releases [5] and classical models [28], the electrostatic field of Fig. 2(a) is dominated by an inward pointing electric field in the interior of the diamagnetic cavity and concentrated near the radial boundary. A second prominent feature, which is not included in idealized models, is the observation of an outward electric field that surrounds the diamagnetic cavity with a magnitude approximately one-third that of the inward field. The reversal of the electric field direction occurs approximately at the
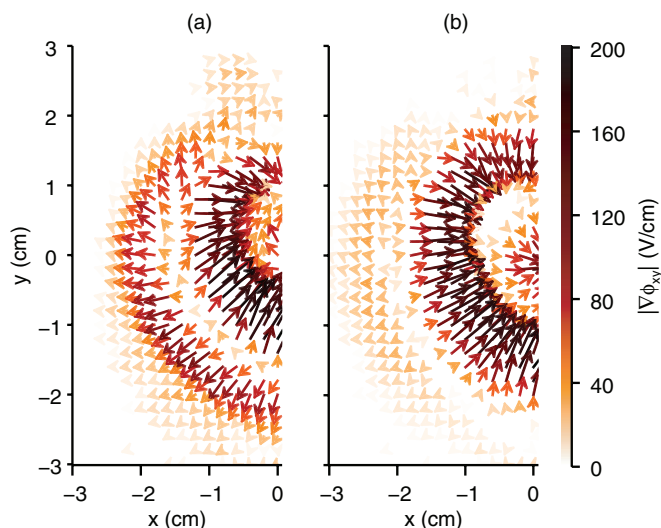

FIG. 2. (Color) Vector plot of electrostatic potential gradients in a plane at $z = 2$ cm (see Fig. 1) for two times (a) $t = 160$ ns and (b) $t = \tau_D = 240$ ns.
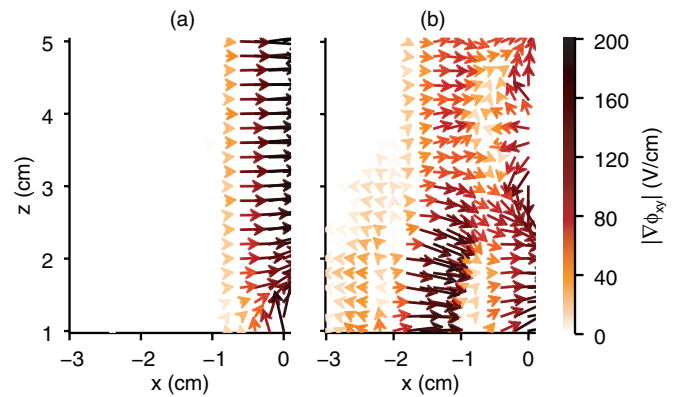

FIG. 3. (Color) Vector plot of electrostatic electric field in a plane at $y = 0$ (see Fig. 1) for times (a) $t = 120$ ns and (b) $t = \tau_D = 240$ ns, with $B_0 = -750\,G\hat{z}$.

cavity edge ($x = 1.5$ cm). To within the resolution of the diagnostics, this is also the location of peak compression in the magnetic field where B_z reaches its maximum value (~ 850 G). Approximately 2 cm away from the axis, the outward electric field drops in magnitude and disappears into the background plasma.

At the time of peak diamagnetism in Fig. 2(b), the electrostatic field appears similar in structure. The inward electric field has maintained its strength and has moved radially outward as the diamagnetic cavity has expanded to $x = 1.8$ cm in the plane. Now, however, the cavity boundary stagnates and no further significant cross-field expansion occurs in either the fields or particles as seen by camera images. The inward electric field persists for the lifetime of the diamagnetic cavity and disappears, falling below 25 V/cm after $t = 600$ ns. The outwardly directed electric field follows the same behavior but diminishes in strength much more rapidly. By peak diamagnetism, it has fallen in strength to ~ 40 V/cm. By $t = 300$ ns, it is too small to measure. The rapid changes in the outward electric field as the cavity passed the probe implied either a dynamic feature of the expansion or possibly the existence of a component of $\vec{\nabla}\phi$ along the background magnetic field. The former is always possible, while the latter could be shown with the diagnostic plane containing the magnetic field. Two such planes are shown in Fig. 3.

At very early times ($t \sim 60$ ns), a 120-V cross-field drop in plasma potential is observed in a narrow [full width at half maximum (FWHM) less than 0.8 cm] field-aligned channel [Fig. 3(a), $t \sim 120$ ns] that persists until the diamagnetic cavity reaches the probe. The drop in potential is coincident with a burst of fast electrons ($v \sim 4 \times 10^8$ cm/s or 50 eV) escaping the LPP. Fast electrons facilitated by neutralizing background electrons have previously been observed using particle diagnostics [4,12] and result in Alfvén and lower-hybrid wave radiation [12,18]. Those experiments were performed using cross-field plasma expansions; here their effect on the plasma potential near the initial laser expansion is measured.

Figure 3(b) shows the electric field of the LPP at the time of peak diamagnetism. Here the LPP leading edge is near $z = 3.2$ cm. Within the diamagnetic cavity, the radial electrostatic field has much the same configuration as that of Fig. 2(b). That is, there exists a strong inward electric field on the inner
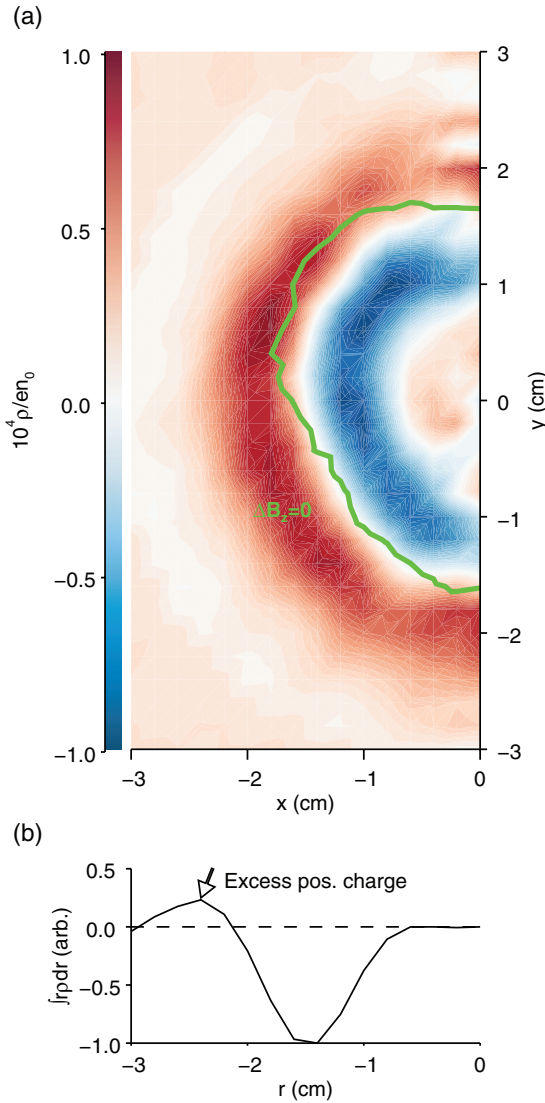
(a)

(b)

FIG. 4. (Color) (a) An xy plane of the calculated charge density relative to en_0 (n_0 is the background density) at $z = 2$ cm. (b) Integrated charge density (normalized) showing a net positive charge of the cavity.

edge of the LPP pointing towards the axis and a radially outward field on the outside edge of the expansion. Note that, although there is a clear axial variation of the electric field, the component $|\partial_z\phi|$ is smaller than $|\partial_r\phi|$ in all regions except the axial boundary of the cavity. At this boundary, the potential structure of the fast electrons gives way to that of the diamagnetic cavity. A parallel electrostatic field here arises to limit the charge carried off by the fast electrons and maintains quasineutral charge balance with the background plasma. Combining the data represented by Figs. 2 and 3, the resultant charge density in a cross section of the diamagnetic cavity can be calculated.

The charge density ρ is calculated using $\partial_x^2\phi + \partial_y^2\phi$ from Fig. 2(b) and $\partial_z^2\phi$ from Fig. 3(b) taking advantage of the azimuthal symmetry of the field in the xy plane. Figure 4(a) shows the result at $z = 2$ cm and $t = 240$ ns. The distribution clearly separates into two layers of excess charge,
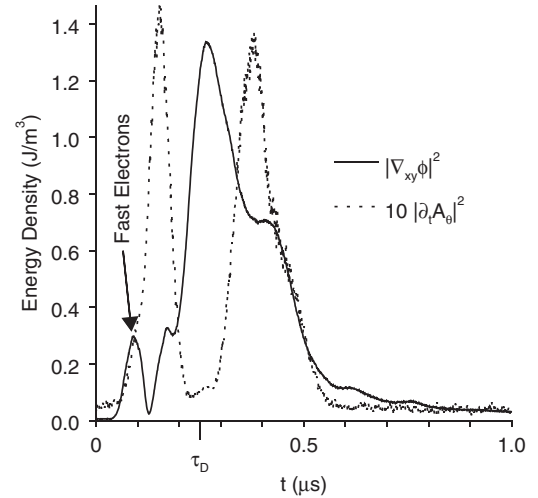

FIG. 5. Comparison of the mean energy density in the electrostatic field and the induced azimuthal electric field (scaled by a factor of 10) as a function of time in the plane $z = 2$ cm.

each with a radial FWHM of 0.8 cm. Though the layers are clearly distinct and responsible for the electrostatic field, they satisfy the quasineutrality condition everywhere—$|\rho/en_0| < 10^{-4}$, where n_0 is the background density. A contour of the instantaneous location of $\Delta B_z = 0$ is superimposed and roughly separates the two charge layers. Integration from 0 to r of the total in-plane charge density [Fig. 4(b)] shows that the positive charge layer is not entirely neutralized by the negative charge layer. Instead, it is eventually neutralized within the background plasma. This structure is consistent with the fast electrons escaping along the magnetic fields lines rendering the diamagnetic cavity positively charged.

Since the electric fields are critical to understanding debris-background ion momentum coupling, it is instructive to directly compare the electrostatic field to the inductive field to gauge their relative importance. A detailed comparison of the 3D evolving structures is an extensive topic, therefore the energy content of their dominant components serves here as the basis for comparison. The dominant component of the induced electric field is that associated with the field expulsion $\partial_t A_\theta$, while that of the electrostatic field is across the background magnetic field $\partial_{xy}\phi$. Figure 5 shows the temporal dependence of the mean energy density of these electric field components in the plane $z = 2$ cm. The electrostatic field is much stronger than the induced field for most of the lifetime of the diamagnetic cavity.

Discussion. In fluid and hybrid simulations of magnetized LPPs, the electric field is calculated via electron momentum balance (or Ohm's law) against thermal and magnetic pressure gradients [29,30]. A comprehensive analysis of the generalized Ohm's law including the spatial and temporal dynamics of the fields is beyond the scope of this paper. Nevertheless, a calculation of the peak values of dominant terms in Ohm's law at a given time is possible. In the laboratory frame, the dominant terms in Ohm's law across the magnetic field are

$$E_r - \frac{[\vec{J} \times \vec{B}]_r}{en_e} + T_e\partial_r \ln n_e - \eta_\perp J_r = 0 \qquad (1)$$

TABLE I. Measured dominant terms in the generalized Ohm's law (in V/cm). Peak values are shown for the experiment to evaluate their relative importance.

Terms	$\vec{E}$	$\vec{V} \times \vec{B}$	$-\vec{J} \times \vec{B}/en_e$	$-T_e \vec{\nabla} \ln n_e$	$-\eta_\perp \vec{J}$
radial	200 ± 20	0	-300 ± 50	-4 ± 2	-10 ± 4
azimuthal	-30 ± 3	100 ± 20	-30 ± 5	0	-50 ± 19

in the radial direction and

$$E_\theta + V_r B_z - \frac{[\vec{J} \times \vec{B}]_\theta}{en_e} - \eta_\perp J_\theta = 0 \qquad (2)$$

in the azimuthal direction, where $\eta_\perp$ is the transverse Spitzer resistivity. An adiabatic expansion model including effects of recombination is used to calculate terms involving the temperature and density that follow $T_e \sim t^{-1}$ and $n_e \sim t^{-3}$ [31,32]. Estimating initial conditions using scaling laws [26], at $t = 200$ ns, the density and temperature are approximately $n_e = 4 \times 10^{13}$ cm^{-3} and $T_e = 1$ eV. Note that such models characterize volume-averaged quantities, so compression by the deceleration at the leading edge of the diamagnetic cavity leads to slightly higher densities and temperatures [33]. The density gradient scale length is determined from CCD images of spontaneous emission where visible emission gradients are dominated by electron density gradients [31]. They show $(\partial_r \ln n)^{-1} \sim 0.25$ cm. A summary of the components of Eqs. (1) and (2) is presented in Table I. Note as a comparison to other experiments that the ratio of the calculated inward electric field (from $\vec{J} \times \vec{B}$ in a simulation) to $\vec{V} \times \vec{B}$ in the AMPTE experiments [5] is ~ 1.5. Within experimental error, Ohm's law is satisfied with the electric fields measured and without the need to invoke an anomalous resistivity.

The azimuthal component of the electric field is believed to be responsible for energy exchange between the LPP debris ions and the background ions via Larmor coupling [2,19,20]. In spherical and cylindrical expansions, these fields arise from $\vec{V} \times \vec{B}$ motion. From the calculations above, the $\vec{V} \times \vec{B}$ contribution to the azimuthal electric field is partially canceled by a combination of the finite resistivity of the cold electrons as well as features neglected in basic fluid models such as loss of electrons along the magnetic field and charge separation at the radial boundary. Both of these in fact contribute to the formation of the observed electrostatic field. The time it takes the azimuthal electric field to cause a radial flow in the ambient

ions is at least 1/4 of their gyroperiod. Hewett *et al.* [20] discussed the complexity of the resultant motion when a finite pulse of an electric field passes a magnetized particle. Without invoking azimuthal electric fields, the radially outward feature of the electrostatic field can directly accelerate ambient ions outward without the need for gyromotion. The strength of the inward electric field also means that particles that do not receive a large enough momentum transfer in the brief passing of the boundary layer will decelerate and become entrained in the diamagnetic cavity. This behavior still amounts to momentum coupling, but no longer does it lead to a traditional shock structure in the limit of large coupling.

Conclusion. Using an emissive probe, the structure of the electrostatic field of a magnetized laser-produced plasma has been measured. This field has two main features across the background magnetic field: an inward field on the interior of the diamagnetic cavity and an outwardly directed field on the exterior. For both directions, the radial electric field spatially corresponds to and is balanced in magnitude by the $\vec{J} \times \vec{B}$ force on the electrons. An estimate of the inductive electric field from magnetic probe data showed it to be smaller than the dominant electrostatic component.

The momentum coupling to the ambient plasma has previously been attributed to Larmor coupling through the induced $\vec{V} \times \vec{B}$ electric fields, while the effect of the electrostatic fields was otherwise neglected. In this experiment we showed that the electrostatic field is not negligible and gives an alternative picture of collisionless momentum coupling in a magnetized plasma expansion with $p_{\rm ram} 2\mu_0/B^2 \gg 1$ and $v_{\rm exp} \sim v_A$.

A different feature revealed in this experiment is the narrow electrostatic structure formed by the fast electrons escaping along the background magnetic field [Fig. 3(a)] that move about 10 times faster than the laser-produced plasma. The wake of the structure persists until the bulk LPP and its diamagnetic cavity disrupt it, resulting in a complicated moving boundary along the magnetic field. This boundary has components of the electrostatic field parallel to the background field, which can result in rapid acceleration of ambient electrons and help explain acceleration of electrons previously observed in similar LPP experiments using the LaPD.

[1] G. Dimonte and L. G. Wiley, Phys. Rev. Lett. **67**, 1755 (1991).

[2] T. P. Wright, Phys. Fluids **14**, 1905 (1971).

[3] M. Van Zeeland, W. Gekelman, S. Vincena, and G. Dimonte, Phys. Rev. Lett. **87**, 105001 (2001).

[4] C. Niemann *et al.*, Phys. Plasmas **20**, 012108 (2013).

[5] P. A. Bernhardt, R. A. Roussel-Dupre, M. B. Pongratz, G. Haerendel, A. Valenzuela, D. A. Gurnett, and R. R. Anderson, J. Geophys. Res. **92**, 5777 (1987).

[6] P. Dyal, J. Geophys. Res. **111**, A12211 (2006).

[7] S. A. Colgate, J. Geophys. Res. **70**, 3161 (1965).

[8] B. E. Goldstein, K. Altwegg, H. Balsiger, S. A. Fuselier, W.-H. Ip, A. Meier, M. Neugebauer, H. Rosenbauer, and R. Schwenn, J. Geophys. Res. **94**, 17251 (1989).

[9] M. F. Thomsen, J. T. Gosling, S. A. Fuselier, and S. J. Bame, J. Geophys. Res. **91**, 2961 (1986).

[10] D. D. Ryutov, R. P. Drake, and B. A. Remington, Astrophys. J. Suppl. Ser. **127**, 465 (2000).

[11] Y. P. Zakharov, IEEE Trans. Plasma Sci. **31**, 1243 (2003).

[12] W. Gekelman, M. Van Zeeland, S. Vincena, and P. Pribyl, J. Geophys. Res. **108**, 1281 (2003).

[13] B. A. Remington, R. P. Drake, H. Takabe, and D. Arnett, Phys. Plasmas **7**, 1641 (2000).

[14] R. P. Drake, Phys. Plasmas **7**, 4690 (2000).

[15] B. H. Ripin, E. A. McLean, C. K. Manka, C. Pawley, J. A. Stamper, T. A. Peyser, A. N. Mostovych, J. Grun, A. B. Hassam, and J. Huba, Phys. Rev. Lett. **59**, 2299 (1987).

[16] A. Collette and W. Gekelman, Phys. Rev. Lett. **105**, 195003 (2010).

[17] A. N. Mostovych, B. H. Ripin, and J. A. Stamper, Phys. Rev. Lett. **62**, 2837 (1989).

[18] S. Vincena, W. Gekelman, M. Van Zeeland, J. Maggs, and A. Collette, Phys. Plasmas **15**, 072114 (2008).

[19] D. B. Schaeffer, E. T. Everson, D. Winske, C. G. Constantin, A. S. Bondarenko, L. A. Morton, K. A. Flippo, D. S. Montgomery, S. A. Gaillard, and C. Niemann, Phys. Plasmas **19**, 070702 (2012).

[20] D. W. Hewett, S. H. Brecht, and D. J. Larson, J. Geophys. Res. **116**, A11310 (2011).

[21] C. Niemann *et al.*, Geophys. Res. Lett. **41**, 7413 (2014).

[22] W. Gekelman, H. Pfister, Z. Lucky, J. Bamber, D. Leneman, and J. Maggs, Rev. Sci. Instrum. **62**, 2875 (1991).

[23] B. Van Compernolle, W. Gekelman, P. Pribyl, and C. M. Cooper, Phys. Plasmas **18**, 123501 (2011).

[24] T. O'Neil and T. K. Fowler, Phys. Fluids **8**, 2255 (1965).

[25] J. W. Poukey, Phys. Fluids **12**, 1452 (1969).

[26] B. Meyer and G. Thiell, Phys. Fluids **27**, 302 (1984).

[27] M. J. Martin, J. Bonde, W. Gekelman, and P. Pribyl, Rev. Sci. Instrum. **86**, 053507 (2015).

[28] Y. P. Raizer, Zh. Prikl. Mekh. Tekh. Fiz. **6**, 19 (1963).

[29] D. Winske and S. P. Gary, J. Geophys. Res. **112**, A10303 (2007).

[30] S. E. Clark, D. Winske, D. B. Schaeffer, E. T. Eveson, A. S. Bondarenko, C. G. Constantin, and C. Niemann, Phys. Plasmas **20**, 082129 (2013).

[31] H. Puell, Z. Naturforsch. **25a**, 1807 (1970).

[32] P. T. Rumsby and J. W. M. Paul, Plasma Phys. **16**, 247 (1974).

[33] S. Sudo, K. N. Sato, and T. Sekiguchi, J. Phys. D **11**, 389 (1978).